



HAL
open science

Molten salt flux synthesis of cobalt doped refractory double perovskite $\text{Sr}_2\text{Co}_x\text{Ga}_{1-x}\text{NbO}_6$: A spectroscopic investigation for multifunctional materials

Maneesha Varghese, Mathieu Duttine, Hitesh Duggal, Nicolas Penin, Eric Lebraud, Alexandre Fargues, Olivier Toulemonde

► To cite this version:

Maneesha Varghese, Mathieu Duttine, Hitesh Duggal, Nicolas Penin, Eric Lebraud, et al.. Molten salt flux synthesis of cobalt doped refractory double perovskite $\text{Sr}_2\text{Co}_x\text{Ga}_{1-x}\text{NbO}_6$: A spectroscopic investigation for multifunctional materials. *Journal of Solid State Chemistry*, 2022, 315, 123507 (10 p.). 10.1016/j.jssc.2022.123507 . hal-03777165

HAL Id: hal-03777165

<https://hal.science/hal-03777165>

Submitted on 14 Sep 2022

HAL is a multi-disciplinary open access archive for the deposit and dissemination of scientific research documents, whether they are published or not. The documents may come from teaching and research institutions in France or abroad, or from public or private research centers.

L'archive ouverte pluridisciplinaire **HAL**, est destinée au dépôt et à la diffusion de documents scientifiques de niveau recherche, publiés ou non, émanant des établissements d'enseignement et de recherche français ou étrangers, des laboratoires publics ou privés.

Molten salt flux synthesis of cobalt doped refractory double perovskite $\text{Sr}_2\text{Co}_x\text{Ga}_{1-x}\text{NbO}_6$: a spectroscopic investigation for multifunctional materials

Maneesha Varghese^{1,1,*}, Mathieu Duttine¹, Hitesh Duggal^{1,II}, Nicolas Penin¹, Eric Lebraud¹,
Alexandre Farges¹, Olivier Toulemonde^{1,†}

¹Univ. Bordeaux, CNRS, Bordeaux INP, ICMCB, UMR 5026, F-33600 Pessac, France

*† Corresponding authors

Email address: *maneesha.varghese@cea.fr, † olivier.toulemonde@icmb.cnrs.fr

Full postal address: ¹ICMCB – UMR5026, 87 Avenue du Docteur Schweitzer, 33608 PESSAC cedex (France)

Abstract

A simple and cost-effective salt synthesis route toward refractory oxides of composition $\text{Sr}_2\text{Ga}_{1-x}\text{Co}_x\text{NbO}_6$ has been carried out. Herein, we report on the refinement of the set of parameters related to heat treatment to stabilize the ordered perovskite for cobalt content, x , ranging from 0.02 to 0.2. The parameters studied were the nature of the flux, the dwell temperature, the dwell time and the cooling rate for a given cobalt precursor. Our study relied on powder X-ray diffraction, UV-visible-near IR (UV-vis-NIR), Electron Spin Resonance (ESR) and Nuclear Magnetic Resonance (NMR) experiments allowing us to better understand the room temperature electronic structure. The tuning of energy gap with the cobalt content, mixed spin state Co^{3+} (Low Spin + Intermediate/High Spin) at room temperature and the brown shades of these materials render them the multifunctionality.

Keywords: Multifunctional material, Double Perovskite, Molten salt flux synthesis, Electron Spin Resonance, Nuclear Magnetic Resonance, UV-vis-NIR spectroscopy

Current Affiliation :

^I Université Grenoble Alpes, CEA, CNRS, IRIG, SyMMES, F-38000 Grenoble

^{II} Univ. Bordeaux, CRPP, CNRS, UPR 8641, 115 Avenue A. Schweitzer, 33600 Pessac, France

Introduction

Despite of the huge contribution of the textile industry on world economy, its contribution to water pollution is also unfortunately undeniable.^{1, 2} The untreated effluent from the textile industry or any chemical industry pollutes water bodies around the world and is a growing threat to aquatic life and thereby to humankind itself. Extensive research has been made in order to purify water polluted by synthetic dye waste discharged all around the world.²⁻⁷ Therefore, remedies are needed to overcome the difficulties put forth by such chemical waste.^{8,9} Unlike several typical methods to treat the polluted water like anaerobic,¹⁰ aerobic,¹¹ oxidation,^{12,13} reduction¹⁴ and so on, photocatalysis is a promising technique which uses simple technology that has proven to have substantial performance.¹⁵⁻²⁰ Doping with transition metal cations has proven to enhance the photocatalytic efficiency of semiconductors.^{21,22} Cobalt is the most efficacious dopant among the different transition metals^{21,23-25} studied so far because its electronic structure aids photocatalytic properties and promotes strong absorption peaks in the visible region of light.²⁶⁻³³ Studies have shown that Co-doped ZnO and Co-doped TiO₂ are much efficient photocatalysts than their pristine counterparts.^{32,34-36} Regardless, it is noteworthy that by contemplating the range of properties shown by oxide perovskites and their derivatives, they can be used in technologies that make use of photocatalysts.³⁷⁻⁴⁰ In addition, studies have shown an enhancement in the photocatalytic properties in oxide perovskites synthesized via flux method.⁴¹⁻⁴⁵ Cobalt was chosen in our study for its spin crossover ability⁴⁶⁻⁴⁸. Thermally induced thermochromism had been reported as well in cobalt substituted oxide perovskites.⁴⁶ And thermochromic materials are used as inorganic pigments for (smart) paintings.⁴⁹⁻⁵² In summary, the Co substituted materials offer multifunctional applications.

Herein, to reduce the synthetic route cost toward phase-pure complex perovskite, an appropriate method leading to the preparation of nanocrystallites and/or microcrystallites is proposed. It is based on molten salt flux growth technique that has been widely used to stabilize crystals large enough in size for many physical property characterizations including studies of magnetic transitions, electrical conductivity, neutron diffraction and optical properties as proposed for some complex oxide⁵³. The idea is to follow such flux synthesis strategy as recently proposed for cobalt or manganese perovskite^{54,55} and to stop the process in a post nucleation state prior to larger crystal growth. Such strategy will allow to significantly lower the thermal treatment temperature used to synthesize derived refractory oxides Sr₂Ga_{1-x}Co_xNbO₆.

Experimental section

Sample preparation: Sr₂Ga_{1-x}Co_xNbO₆ double perovskite samples were grown via flux (molten-salt) method. First of all, SrCO₃ was dried by following a thermal treatment at 200°C. Co₃O₄ was prepared from cobalt acetate by heating it at 650°C for 12 hours with a heating and cooling rate of 5°C/min. Stoichiometric amounts of dried SrCO₃, Co₃O₄, Ga₂O₃ and Nb₂O₅ were mixed in order to achieve a

molar ratio of Sr:Co:Ga:Nb = 2 : x/3 : (1-x)/2 : 1/2, where x is the molar content of cobalt. Thereafter, the reactants were mixed with the salt flux in flux/product mass ratio, y, ranging from 1 to 4. The reactants-flux mixture was then heated in air to a fixed temperature in the range between 900°C – 1100°C at a heating rate of 5°C/min, held from 8 to 72 hours and followed by cooling to room temperature at different cooling rates from 5°C/min to 0.2°C/min. The products were thoroughly washed with an acidified distilled water to remove the flux and dried at room temperature for 48 hours.

Instrumental details: The room temperature (RT) powder X-ray diffraction (PXRD) patterns – routine mode – were collected using a PANalytical X'Pert MPD PRO diffractometer equipped with a secondary monochromator. The diffractograms were measured over an angular range of 2θ from 8° to 80° with a step size of 0.016° in Bragg-Brentano θ - θ geometry with copper $K\alpha$ radiation ($\lambda = 1.5418 \text{ \AA}$).

The $K\alpha_1$ data collection to perform Rietveld refinement was carried out using PANalytical X'Pert MPD PRO diffractometer equipped with Cu- $K\alpha_1$ Ge – 111 monochromator ($\lambda = 1.540598 \text{ \AA}$) in Bragg-Brentano θ - 2θ geometry over the 2θ range of 10°–130° with a step size of 0.008°.

Bruker ESP300E spectrometer operating at X-band frequency (9.54 GHz) equipped with a liquid helium flow cryostat was used to record Electron Spin Resonance (ESR) powder spectra from ambient temperature down to 5 K. The main spectroscopic parameters used to obtain the reported spectra are microwave power of 10 mW, magnetic field modulation frequency of 100 kHz and amplitude of 1 mT, spectral resolution of 0.65 G/point and a conversion time of 82 ms. The spectrometer was calibrated (in magnetic field) using an external reference sample of *DPPH* ($g = 2.0036$).

^{93}Nb ($I = 9/2$) and ^{59}Co ($I = 7/2$) Nuclear Magnetic Resonance (NMR) spectra were recorded under Magic Angle Spinning (MAS) conditions on a Bruker Avance III 300WB solid-state spectrometer (7.05 T) using a 2.5 mm MAS DVT probe with a typical 30 kHz spinning frequency. For both nuclei, single pulse experiments were performed with a $\pi/20$ pulse length of 1.26 μs and a $\pi/16$ pulse length of 1 μs , respectively and an optimized recycle delay of 0.5 s. Saturated solution of NbCl_5 (in CH_3CN) and 0.1M solution of $\text{K}_3[\text{Co}(\text{CN})_6]$ were used as external reference samples for the ^{93}Nb and ^{59}Co NMR shifts (expressed in ppm). ^{71}Ga ($I = 3/2$) MAS NMR spectra were recorded on a Bruker Avance III 500WB solid-state spectrometer (11.7 T) using a 1.3 mm MAS probe with a MAS rate of 60 kHz, a short $\pi/8$ pulse length of 1.05 μs and an optimized recycle delay of 1 s. Gallium Arsenide (GaAs ; $\delta_{\text{iso.}} = -215 \text{ ppm}$) was used as solid reference sample for the ^{71}Ga NMR shifts (expressed in ppm).

UV-vis-NIR diffuse reflectance spectra were recorded using Agilent Cary 5000 spectrophotometer in the wavelength range of 200 nm – 1500 nm at room temperature. A step size of 1 nm was used for 200

nm – 800 nm range and 2 nm for 800 nm – 1500 nm range. Halon was used as a white reference to calibrate the spectrometer.

Results

Double perovskite formation and phase purity of the samples were first investigated using X-ray powder diffraction in a routine mode. Results are sequentially shown following the different studied parameters. For the sake of clarity, all the following analysis are proposed for $\text{Sr}_2(\text{Co}_{0.04}\text{Ga}_{0.96})\text{NbO}_6$ compositions. The latter, namely $x = 0.04$ were prepared by mixing stoichiometric amount of precursors in a mortar and pestle along with the SrCl_2 flux in a 2:1 flux:product ratio by using Co_3O_4 as the cobalt precursor. Subsequently, the impact of varying cobalt content, x is presented for some selected set of parameters.

a) Nature of flux

For a fixed cobalt content $x = 0.04$, the nature of flux investigated were SrCl_2 , NaCl , KCl , BaCl_2 , $\text{NaCl} + \text{KCl}$, $\text{BaCl}_2 + \text{KCl}$. The flux:product ratio was arbitrarily chosen to be 2:1, i.e., 2 g of flux was added for each gram of product prepared. For the eutectic mixing of flux ($\text{NaCl} + \text{KCl}$, $\text{BaCl}_2 + \text{KCl}$), the two salt fluxes were taken in a 1:1 ratio and the temperature of melting and boiling were found from their respective phase diagrams. The nature of flux used as well as with their melting and boiling points are given in Table. 1.

Flux Used	Flux: Sample Ratio	Melting Point (°C)	Boiling Point (°C)
SrCl_2	2:1	874	1250
NaCl	2:1	801	1465
KCl	2:1	771	1420
BaCl_2	2:1	962	1560
$\text{KCl} + \text{NaCl}$ (1:1)	2:1	657	1443
$\text{BaCl}_2 + \text{KCl}$ (1:1)	2:1	900	1490

Table. 1: Nature of flux used for $\text{Sr}_2(\text{Co}_{0.04}\text{Ga}_{0.96})\text{NbO}_6$ sample preparation, flux:sample ratio and the corresponding melting and boiling points.

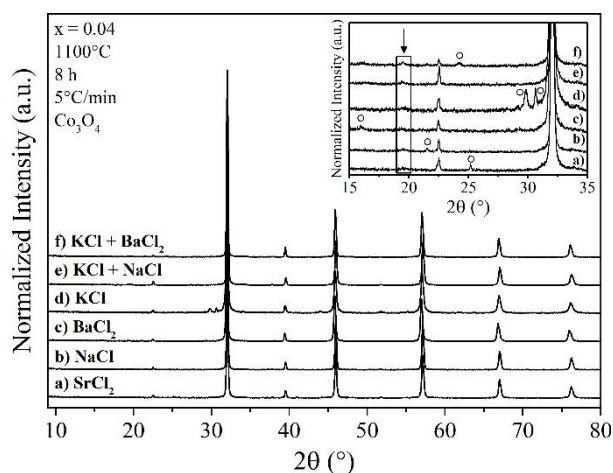


Fig.1: Room temperature X-ray diffraction patterns of the $\text{Sr}_2(\text{Co}_{0.04}\text{Ga}_{0.96})\text{NbO}_6$ samples depending on the nature of flux used. Inset: The arrow underlines the superstructure peak at $\sim 19^{\circ}$ whereas \circ (circles) show impurity peaks.

The RT PXRD patterns corresponding to the $\text{Sr}_2(\text{Co}_{0.04}\text{Ga}_{0.96})\text{NbO}_6$ double perovskite stabilized using different types of flux is shown in Fig. 1. The ordering in these double perovskites can be pointed out by the appearance of superstructure peaks, for example, the (111) diffraction line is underlined in the inset by an arrow. Also, some of the prepared $\text{Sr}_2(\text{Co}_{0.04}\text{Ga}_{0.96})\text{NbO}_6$ samples had shown unknown impurity peaks along with the double perovskite formation. Although, it is shown that the KCl + NaCl (1:1) flux do not stabilize any detected impurity in the routine mode RT XRD, SrCl₂ flux was selected for the preparation of samples. Indeed, the A-site cation of the double perovskite studied ($\text{Sr}_2(\text{Co}_x\text{Ga}_{1-x})\text{NbO}_6$) and the cation of the salt flux SrCl₂ are the same which would prevent introducing unwanted impurities by the reaction of precursors and the cation of the salt flux. It has to be noted that the flux:product ratio for the synthesis of $\text{Sr}_2(\text{Co}_x\text{Ga}_{1-x})\text{NbO}_6$ double perovskites was also studied as shown in Supplementary Information Fig. S1 confirming the optimized 2:1 flux:product ratio.

b) Dwell temperature

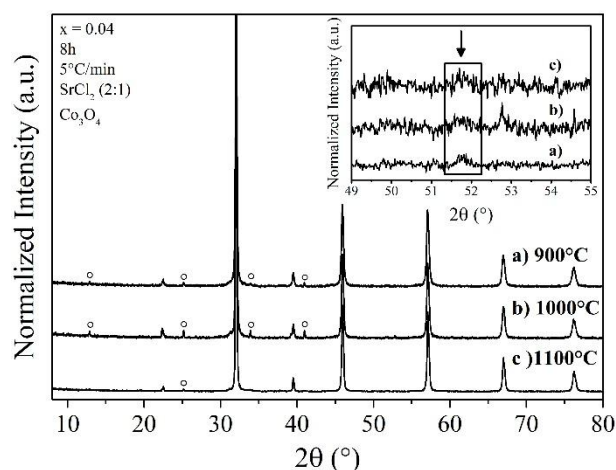


Fig. 2. Room temperature X-ray diffraction patterns of $\text{Sr}_2(\text{Co}_{0.04}\text{Ga}_{0.96})\text{NbO}_6$ prepared by varying dwell temperature of the thermal cycle. ° markers correspond to the unknown impurities found and the inset shows the zoomed superstructure peak at $\sim 51.8^\circ$ (marked with an arrow).

The next studied parameter for the heat treatment was the dwell temperature. The choice of dwell temperatures for the study (900°C, 1000°C, 1100°C) was based on the melting and boiling point of SrCl_2 (see Table. 1). The other heat treatment parameters which were kept unchanged from the previous section are flux:product ratio as 2:1, the dwell time of 8 hours and the cooling rate of 5°C/min. The mixture of reactants and flux was then heated at 900°C, 1000°C and 1100°C using the aforementioned other heat treatment parameters. The RT PXRD patterns of the double perovskite $\text{Sr}_2(\text{Co}_{0.04}\text{Ga}_{0.96})\text{NbO}_6$ prepared at 900°C, 1000°C and 1100°C are shown in Fig. 2 with the inset showing the superstructure peak at $\sim 51.8^\circ$ (as the normalized superstructure peak intensity at $\sim 19^\circ$ was indistinct). Unexpectedly, it was seen that the PXRD pattern of sample prepared at 1000°C showed more content of unknown impurity than the other two. Dwell temperature of 1100°C seems to be the optimized temperature to reach $\text{Sr}_2(\text{Co}_{0.04}\text{Ga}_{0.96})\text{NbO}_6$ double perovskite. However, $\text{Sr}_2(\text{Co}_{0.04}\text{Ga}_{0.94})\text{NbO}_6$ double perovskite prepared at 1100°C for 8h using at 5°C/min cooling rate was unfortunately not pure from the refinement of Rietveld high resolution data collection as is shown in supplementary information (Fig. S2 & Table S1). For the rest of the parameter change study, 900°C was opted as the dwell temperature having in mind that flux method is used to reduce the time and cost of the synthesis and therefore, both the dwell temperature and dwell time of the heat treatment need to be reduced to obtain desired products. This is also the reason for exploring the effect of kinetic parameter, i.e., the dwell time parameter of the heat treatment. For the purpose, the reactants and salt flux mixture in 2:1 flux:product ratio was heated at 900°C at 8 hours, 40 hours, and 72 hours at a heating and cooling rate of 5°C/min.

c) Dwell time

Fig. 3 shows the RT PXRD patterns of the samples prepared by varying the dwell time of the thermal cycle. The longer the dwell time is, the better the B-site cation ordering is. This can be easily perceived from the inset of Fig. 3, that the superstructure peak relating to the ordering in the double perovskite was more intense for the dwell time of 72 hours compared to the other dwell times studied. The impurity content was seen to decrease when the dwell time was decreased from 40 hours to 8 hours. Perhaps, the possible reason for the impurity content to decrease is a threshold dwell time after which the impurity phase starts to disintegrate and all the phases (impurity phase and the desired phase) start to merge to one phase, the kinetically favoured stable phase. That is, the longer the dwell time is, the longer the time available for the kinetically stable phase to get stabilized.

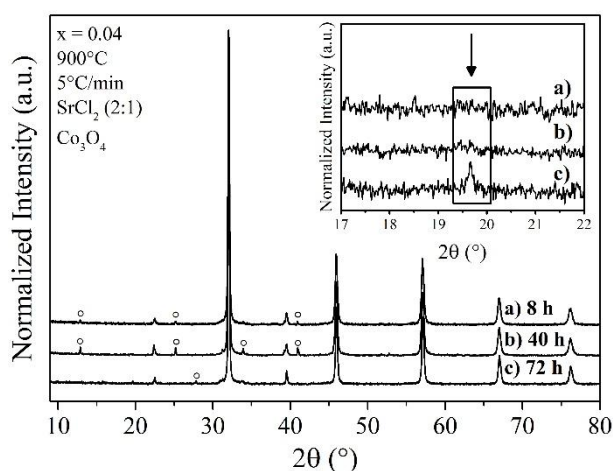


Fig. 3: Room temperature X-ray diffraction patterns of $\text{Sr}_2(\text{Co}_{0.04}\text{Ga}_{0.96})\text{NbO}_6$ prepared by varying dwell time of the thermal cycle. ° markers correspond to the unknown impurities found and the inset shows the zoomed superstructure peak at $\sim 19.6^\circ$ (marked with an arrow).

d) Cobalt content (x)

At this stage, in order to further study if the cobalt content has an impact on ordering, $\text{Sr}_2(\text{Co}_x\text{Ga}_{1-x})\text{NbO}_6$ double perovskite was prepared by varying x where $x = \{0.02, 0.04, 0.08, 0.12, 0.20\}$. Stoichiometric amounts of precursors were mixed in a mortar using a pestle along with SrCl_2 flux at 2:1 flux:product ratio. The mixture was then heated at 900°C for 8 hours at a heating and cooling rate of $5^\circ\text{C}/\text{min}$. Fig. 4 shows the RT PXRD patterns of $\text{Sr}_2(\text{Co}_x\text{Ga}_{1-x})\text{NbO}_6$ double perovskites with varying cobalt content, x. Unknown impurity phase(s) was(were) found in RT PXRD for all the samples prepared. Nevertheless, the content of impurity is really low for the samples prepared with cobalt content, $x = 0.02, 0.04$ and 0.08 in the routine mode PXRD pattern. As the superstructure peaks were hard to be discerned because of the high signal to noise ratio, the superstructure peaks are not highlighted in Fig. 4.

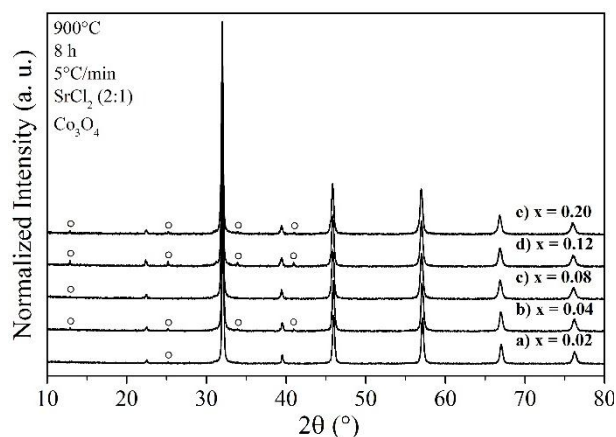


Fig. 4: Room temperature X-ray diffraction patterns of $\text{Sr}_2(\text{Co}_x\text{Ga}_{1-x})\text{NbO}_6$ double perovskites prepared with varying cobalt content, x .

e) Cooling rate

Finally, the cooling rate effect was studied for a set of cobalt content ($x = 0.02, 0.04$ and 0.08). The flux method of synthesis is commonly and mainly used for the single crystal growth^{56–59} for which usually the dwell time is longer and the cooling rate is slower of the heat treatment. Hence, $\text{Sr}_2(\text{Co}_x\text{Ga}_{1-x})\text{NbO}_6$ double perovskite were prepared by heating the mixture of precursors and SrCl_2 flux (2:1 flux:product ratio) at 900°C for 72 hours as just suggested with a slow cooling rate, $0.2^\circ\text{C}/\text{min}$. The RT PXRD patterns of $\text{Sr}_2(\text{Co}_x\text{Ga}_{1-x})\text{NbO}_6$ double perovskites ($x = 0.02, 0.04, 0.08$) prepared using long dwell time and slow cooling rate varying the cobalt content is shown in Fig. 5. Presence of ordering is observed in all the samples prepared which was proved by the observance of superstructure peaks. The superstructure peaks – at $\sim 19^\circ$ i.e. (111) peak and $\sim 38^\circ$ i.e. (311) peak – are shown in the inset figure of Fig. 5. However, $\text{Sr}_2(\text{Co}_x\text{Ga}_{1-x})\text{NbO}_6$ double perovskite with $x = 0.02, 0.08$ showed unknown impurity peaks in the PXRD patterns unlike $\text{Sr}_2(\text{Co}_{0.04}\text{Ga}_{0.96})\text{NbO}_6$ double perovskite that can be reduced increasing the dwell time.

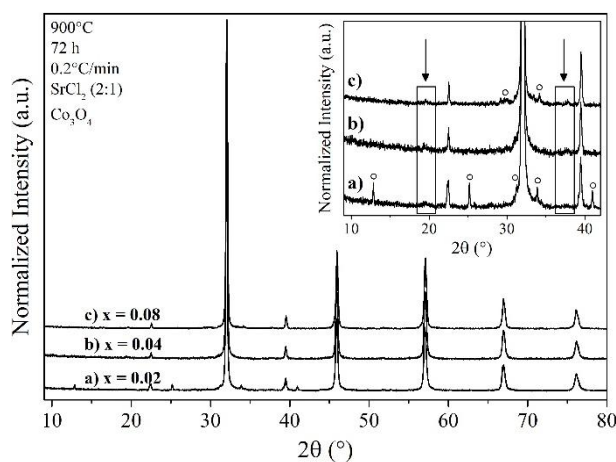


Fig. 5: Room temperature X-ray diffraction patterns of $\text{Sr}_2(\text{Co}_x\text{Ga}_{1-x})\text{NbO}_6$ double perovskite ($x = 0.02, 0.04, 0.08$) prepared using a slow cooling rate ($0.2^\circ\text{C}/\text{min}$).

Therefore, the best parameters for heat treatment using flux (SrCl_2 in 2:1 flux:product ratio) mediated synthesis to stabilize $\text{Sr}_2\text{Co}_x\text{Ga}_{1-x}\text{NbO}_6$ double perovskite was found to be as the cobalt content, $x = 0.04$ prepared at 900°C dwell temperature with 72 hours dwell time and a slow cooling rate of $0.2^\circ\text{C}/\text{min}$. In the following paragraphs, the structural and spectroscopic results of this so prepared phase-pure sample are discussed. Additionally, UV-vis-NIR spectroscopic analysis of $\text{Sr}_2\text{Co}_x\text{Ga}_{1-x}\text{NbO}_6$ double perovskite is discussed under the scope of these materials to be potential photocatalysts for water splitting.^{39,60}

Nuclear Magnetic Resonance & Electron Spin Resonance:

To study the potentiality of $\text{Sr}_2\text{Co}_{0.04}\text{Ga}_{0.96}\text{NbO}_6$ as thermal sensors/switch which manifest thermally induced thermochromism, Nuclear Magnetic Resonance (NMR) and Electron Spin Resonance (ESR) as local probes were carried out. The lowest cobalt content was selected to perform such study. Furthermore, because NMR spectroscopy is sensitive to low spin Co^{3+} (LS: $t_2g^6 eg^0$) ion and ESR to high spin/intermediate spin Co^{3+} (HS: $t_2g^4 eg^2$ / IS: $t_2g^5 eg^1$), both experiments should allow us to probe the electronic nature of the cobalt in the double perovskite under study.

^{59}Co , ^{71}Ga and ^{93}Nb MAS NMR spectroscopy was used to locally probe the different cationic environments. ^{59}Co and ^{71}Ga spectra with spinning side bands manifold can be found in Fig. S3. The isotropic lines of the ^{59}Co , ^{71}Ga and ^{93}Nb NMR spectra may be considered as the sum of several resonance lines with Gaussian line shape (Fig. 6) that are associated with different local environments for the three probed nuclei. Indeed, the slight changes in isotropic shift value are mainly due to the distribution of Ga^{3+} and Co^{3+} (LS and IS/HS) around Nb, Ga and Co ions in the double perovskite structure.⁶¹ The main resonance line (peak 1) corresponds to the more regular environment (regarding first and second neighbour cationic distribution) that is, for instance, Nb ions surrounded by only Nb and Ga ions by only Ga ions. Depending on the spin state and the amount of Co^{3+} ions in the vicinity of Nb, the ^{93}Nb NMR resonance line may be shifted towards higher or lower shift values. The ^{71}Ga and LS- ^{59}Co NMR spectra can be described following the same analysis. Interestingly, the deconvolution of the ^{59}Co and ^{71}Ga MAS NMR spectra (using same width Gaussian subpeaks) are very similar with two subpeaks towards higher shift values and six towards lower shift values suggesting that both ions have almost identical local environment and thus, that the Co ions are located at the Ga-site as desired.

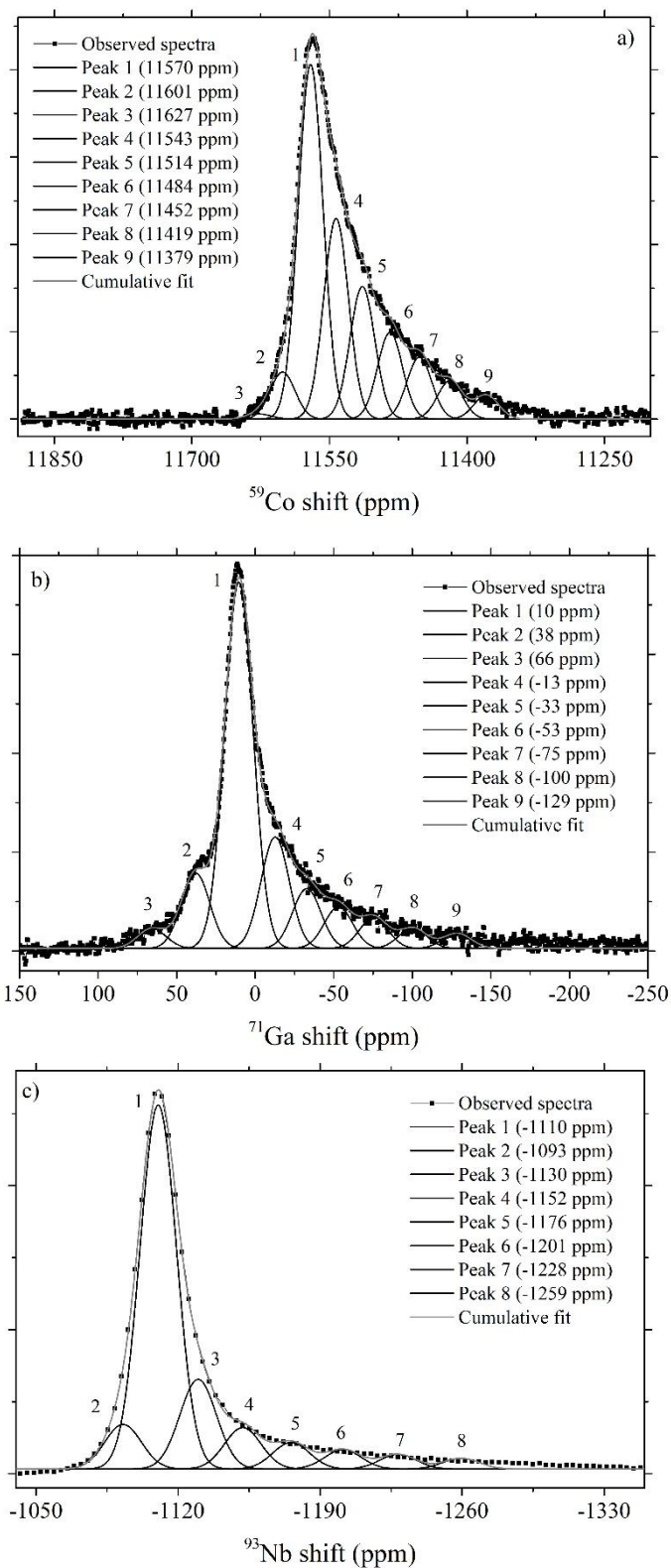


Fig. 6: a) ^{93}Nb and b) ^{59}Co MAS NMR spectra ($B_0 = 7.05$ T; MAS rate 30 kHz) and c) ^{71}Ga MAS NMR spectrum ($B_0 = 11.7$ T; MAS rate 60 kHz) of $\text{Sr}_2(\text{Co}_{0.04}\text{Ga}_{0.96})\text{NbO}_6$ double perovskite.

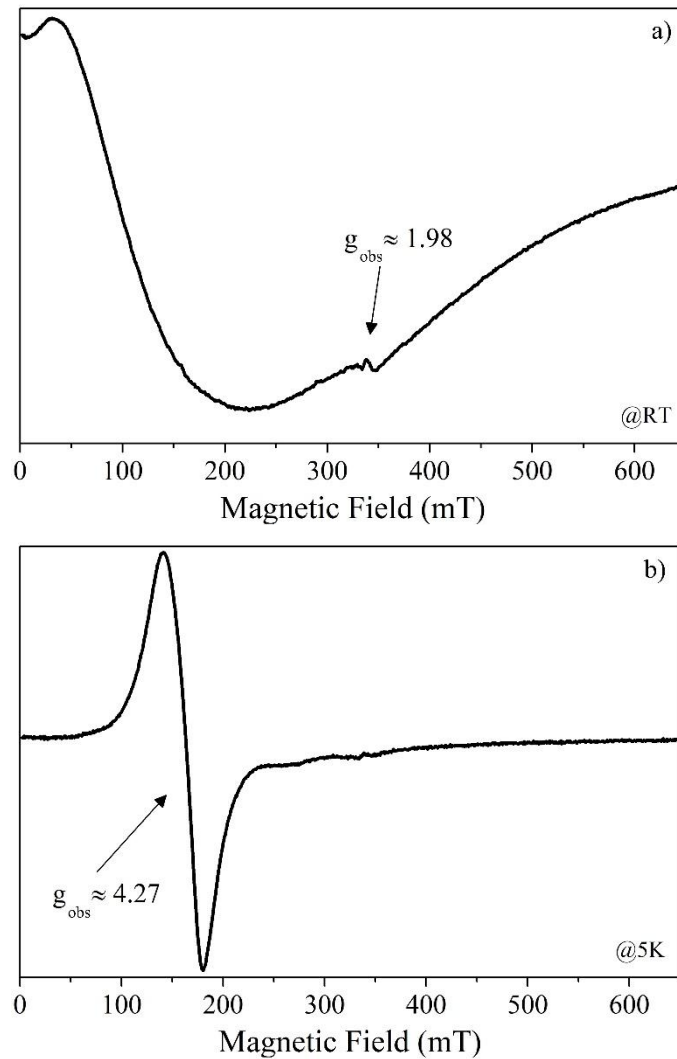


Fig. 7: X-band (9.54 GHz) ESR spectra of $\text{Sr}_2(\text{Co}_{0.04}\text{Ga}_{0.96})\text{NbO}_6$ double perovskite (900°C, 72 hours, cooling rate 0.2°C/min) recorded at a) room temperature (293 K) and b) 5 K and marked with the main observed g -values.

X-band ESR spectra collected for $\text{Sr}_2(\text{Co}_{0.04}\text{Ga}_{0.96})\text{NbO}_6$ double perovskite (900°C, 72h, 0.2°C/min) at room temperature and 5 K is shown in Fig. 7 (a & b respectively). The RT ESR signals match with previous report for LaCoO_3 perovskites^{54,62}. The RT ESR spectrum exhibits a broad and intense signal at low fields and a weak signal at $g \sim 1.98$. The origin of this last signal is not clear but could be related to some oxygen vacancies whereas the broad signal could be due to some traces of unreacted Co_3O_4 . However, no signal at ~ 280 mT⁶³ was detected suggesting that this resonance line could also be attributed to an intrinsic paramagnetic signal originated from IS/HS Co^{3+} . At low temperature (below 30 K), only an intense signal associated with IS or HS Co^{3+} is observed at $g \sim 4.27$.

Along with the NMR experiments revealing the presence of Co^{3+} at the low-spin state, ESR confirms that a part of the Co^{3+} ions in the sample are paramagnetic, i.e., with a high spin or intermediate spin state. Therefore, it can be said that $\text{Sr}_2\text{Co}_{0.04}\text{Ga}_{0.96}\text{NbO}_6$ shows a mixed spin state with a potentiality for thermally induced thermochromic property.

Rietveld Refinement:

Rietveld refinement of PXRD pattern ($K\alpha_1$ data) was used to investigate the credibility of the crystal structure deduced using NMR with the Co distributed at the Ga-site. The structure was surprisingly found to be $Fm\bar{3}m$ whereas the Sr_2CoNbO_6 double perovskite was found to be crystallized in $I4/m$ tetragonal space group but with a slight tetragonal distortion⁶⁴. The observed PXRD pattern, calculated pattern using $Fm\bar{3}m$ and the difference (Observed – Calculated) patterns are shown in Fig. 8 along with the Bragg reflections for the $Fm\bar{3}m$ space group marked with | markers. The approach for the Rietveld refinement performed using TOPAS software is explained in the following paragraph.

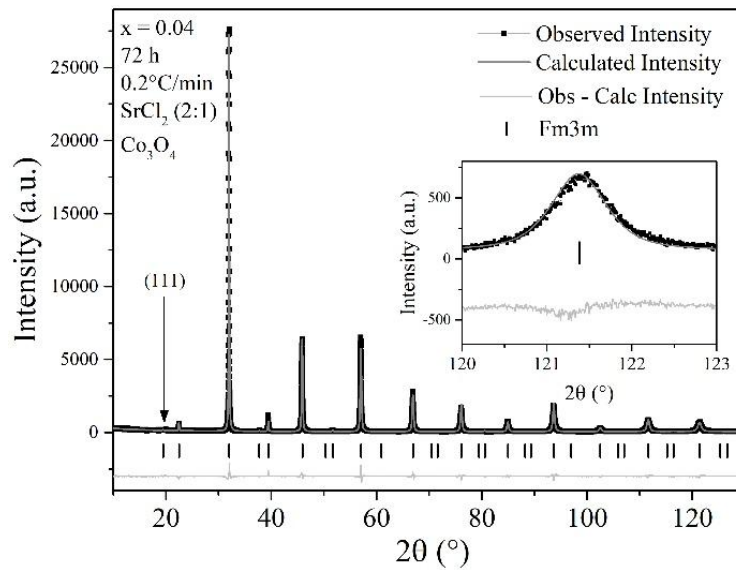


Fig. 8: Observed room temperature X-ray diffraction pattern of $Sr_2(Co_{0.04}Ga_{0.96})NbO_6$ double perovskite for Rietveld refinement (black line+scatter), calculated X-ray diffraction pattern using $Fm\bar{3}m$ space group (grey plot) and difference curve between the observed and calculated X-ray diffraction patterns (little grey plot). | markers indicate the Bragg reflections corresponding to $Fm\bar{3}m$ space group. Inset shows the high angle peak showing the peak symmetry proving $Fm\bar{3}m$ space group crystallization.

As the charge difference between Ga^{3+} and Nb^{5+} is exactly equal to two, a partial ordering of the Ga/Nb octahedra is expected.^{65–67} Whence two structural models for refining RT PXRD could be put forth: model (a) with a mixture of ordered ($Fm\bar{3}m$) and disordered ($Pm\bar{3}m$) phases⁶⁸ and model (b) with fractional occupancy of Ga^{3+}/Nb^{5+} ions in an ordered phase ($Fm\bar{3}m$). PXRD calculated using model (b) fitted the observed PXRD pattern better than the calculated one using model (a). Especially, the peak shape difference between main perovskite peaks and superstructure ones due to B/B' ordering was not well accounted in model (a) (see Fig. S4). The fractional occupancy of Co^{3+} was kept constant as 0.16 (for $x = 0.04$). There were two assumptions made: (1) Co^{3+} occupied Ga^{3+} site as probed in our NMR experiment, (2) the content of cobalt in the final product experimentally produced is equal to the

targeted one, i.e., $x = 0.04$. The original Ga^{3+} site (0.5, 0.5, 0.5) will have 0.16 parts fractionally occupied by Co^{3+} , y parts fractionally occupied by Ga^{3+} and $1-y-0.16$ parts fractionally occupied by Nb^{5+} . And the original Nb^{5+} site (0, 0, 0) will have $y-0.16$ parts of total occupancy for Nb^{5+} , the rest $1-y-0.16$ parts fractionally occupied by Ga^{3+} . Rietveld refinement result is tabulated in Table. 2. And the stable phase-pure $\text{Sr}_2(\text{Co}_{0.04}\text{Ga}_{0.96})\text{NbO}_6$ double perovskite that was crystallized in $Fm\bar{3}m$ space group has 38% B-site cation ordering; the degree of ordering can be calculated using the order parameter, $S = 2z-1$ (where z is the highest fractional occupancy between B and B' cations)⁶⁵.

Site	Wyckoff position	x	y	z	Atom	Occupancy	Beq
$Fm\bar{3}m$; $a = 7.90$ (1) Å							
Rwp = 10.11 and $\chi^2 = 1.41$							
Sr	8	0.25	0.25	0.25	Sr^{2+}	1	0.88 (1)
Ga	4	0.5	0.5	0.5	Ga^{3+}	0.53 (1) [†]	0.05 (4) ^{††}
					Nb^{5+}	0.31 (1) [†]	0.05 (4) ^{††}
					Co^{3+}	0.16	0.05 (4) ^{††}
Nb	4	0	0	0	Nb^{5+}	0.69 (1) [*]	0.05 (4) ^{**}
					Ga^{3+}	0.31 (1) [*]	0.05 (4) ^{**}
O	24	0.2530 (5)	0	0	O^{2-}	1	1.20 (4)

Table. 2. Lattice parameters, atomic positions, isotropic thermal displacements and occupancies for $\text{Sr}_2(\text{Co}_{0.04}\text{Ga}_{0.96})\text{NbO}_6$ double perovskite acquired from PXRD Rietveld refinement using TOPAS. †, ††, *, ** indicate that there were constraints imposed: (a) †Occupancy of Ga^{3+} + Occupancy of Co^{3+} + Occupancy of $\text{Nb}^{5+} = 1$ and *Occupancy of Nb^{5+} + Occupancy of $\text{Ga}^{3+} = 1$, (b) ††, ** Beq at these sites were constrained to be equal.

UV-vis-NIR spectroscopy:

UV-vis-NIR spectroscopy was performed to (i) confirm the mixed spin state in the $\text{Sr}_2\text{Co}_{0.04}\text{Ga}_{0.96}\text{NbO}_6$ double perovskite, and (ii) to study the potentiality of $\text{Sr}_2\text{Co}_x\text{Ga}_{1-x}\text{NbO}_6$ as photocatalyst materials for water splitting. Diffuse absorption was calculated by using absorption, $A(\%) = 100 - R(\%)$ where $R(\%)$ is the reflection in percentage.

(i) $\text{Sr}_2\text{Co}_{0.04}\text{Ga}_{0.96}\text{NbO}_6$

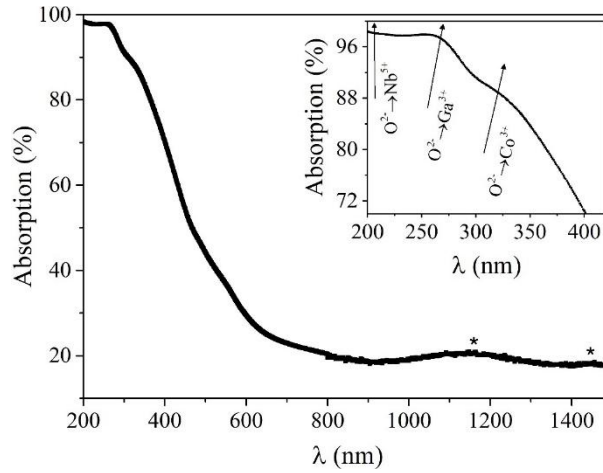


Fig. 9: Room temperature UV-vis-NIR spectra of $\text{Sr}_2\text{Co}_{0.04}\text{Ga}_{0.96}\text{NbO}_6$ double perovskite prepared at 900°C dwell temperature, 72 hours dwell time and $0.2^\circ\text{C}/\text{min}$ cooling rate using SrCl_2 with 2:1 flux:product ratio.

Fig. 9 shows the UV-vis-NIR absorption spectra in the range of 200 nm – 1500 nm of $\text{Sr}_2\text{Co}_{0.04}\text{Ga}_{0.96}\text{NbO}_6$ double perovskite synthesized at 900°C dwell temperature, 72 hours of dwell time and $0.2^\circ\text{C}/\text{min}$ cooling rate using SrCl_2 flux in 2:1 flux:product ratio. The inset of Fig. 9 shows the zoomed part of absorption spectra from 200 nm – 420 nm where the arrows are indicator of the oxygen-to-metal charge transfer observed in these samples. The charge transfer band corresponding to the $\text{O}^{2-} \rightarrow \text{Nb}^{5+}$ have a maximum in the absorption curve in the wavelength range less than 200 nm and the observance of maximum getting to reduce is only visible in the recorded UV-vis-NIR spectra. The charge transfer bands are observed with onsets starting from ~ 250 nm corresponding to $\text{O}^{2-} \rightarrow \text{Ga}^{3+}$ and ~ 330 nm to $\text{O}^{2-} \rightarrow \text{Co}^{3+}$. Moreover, the observance of features in NIR range (marked as \star in Fig. 9) corresponds to the Jahn-Teller distortion. The energy corresponding to the wavelength 1150 nm and 1450 nm that are marked with \star is 1.1 eV and 0.85 eV respectively. The energy between the e_g orbitals, Δ_e for oxides due to HS/IS Co^{3+} is as same for fluorides and it range from ~ 0.3 eV to ~ 1 eV. For the double perovskites under study, $\Delta_e \cong 1.1 - 0.85 = 0.25$ eV, which close to the earlier reported works of fluorides/oxides containing HS/IS Co^{3+} which manifest Jahn-Teller distortion in the samples.⁶⁹

The d-d transitions are poor in intensity in contrast to the Co-doped LaGaO_3 perovskite that was showing clear d-d transition peaks corresponding to the LS Co^{3+} at ~ 500 nm and ~ 700 nm and to the HS Co^{3+} at ~ 550 nm.⁴⁶ However, as there is a mixture of LS + HS/IS Co^{3+} in $\text{Sr}_2\text{Co}_{0.04}\text{Ga}_{0.96}\text{NbO}_6$ under study (900°C , 72h, $0.2^\circ\text{C}/\text{min}$), but the indistinguishable maxima in the absorption spectra due to the possible overlap of d-d transition peaks makes the assignment of peaks to the proper d-d transition an intricate task. Hence, the second derivative of absorption from 400 nm – 700 nm was calculated and is shown in Fig. 10. d-d transitions which give maxima in the UV-vis-NIR spectra (Gaussian peaks) will give minima in the second derivative of absorption.

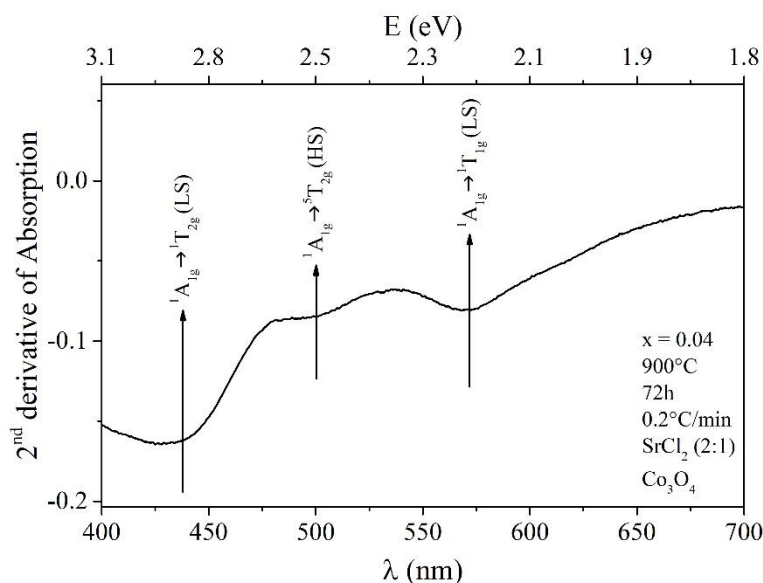


Fig. 10: Second derivative of absorption plot of $\text{Sr}_2\text{Co}_{0.04}\text{Ga}_{0.96}\text{NbO}_6$ double perovskite prepared at 900°C dwell temperature, 72 hours dwell time and $0.2^\circ\text{C}/\text{min}$ using SrCl_2 flux in 2:1 flux:product ratio. The arrows represent different Co^{3+} spin states observed in the sample.

Fig. 10 shows the second derivative plot of absorption spectra versus the wavelength of light used (400 nm – 700 nm; visible range of light) of the recorded spectra of $\text{Sr}_2\text{Co}_{0.04}\text{Ga}_{0.96}\text{NbO}_6$ double perovskite (900°C , 72h, $0.2^\circ\text{C}/\text{min}$). The comparison of second derivative plot of UV-vis-NIR spectra with earlier reported $\text{Sr}_2\text{Co}_{0.02}\text{Ga}_{0.98}\text{NbO}_6$ ⁶¹ and Co-doped LaGaO_3 ⁴⁶ showed that the double perovskite under study has a mixed spin state at room temperature, and the so assigned d-d transition peaks are shown in Fig. 10. The allowed d-d transitions $^1\text{A}_{1g} \rightarrow ^1\text{T}_{2g}$ (~438 nm), $^1\text{A}_{1g} \rightarrow ^1\text{T}_{1g}$ (~572 nm) corresponding to LS Co^{3+} and the $^1\text{A}_{1g} \rightarrow ^5\text{T}_{2g}$ (~499 nm) transition corresponding to the HS Co^{3+} . The UV-vis-NIR spectra analysis underpins the observance of HS/IS Co^{3+} from the ESR and LS Co^{3+} from the NMR spectroscopic results.

$\text{Sr}_2\text{Co}_x\text{Ga}_{1-x}\text{NbO}_6$

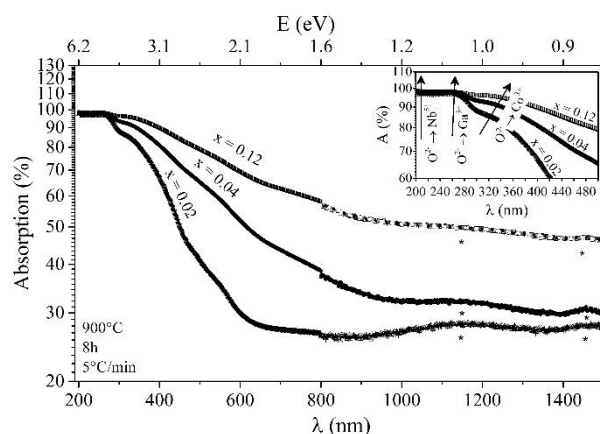


Fig. 11: UV-vis-NIR absorption spectra obtained after transformation of the diffuse reflectance spectra considering the absorption percentage such as: $A\% = 100 - R_{\text{diff}}\%$.

The optical properties of some of the $\text{Sr}_2(\text{Co}_x\text{Ga}_{1-x})\text{NbO}_6$ ($x = 0.02, 0.04$ and 0.12) double perovskites prepared were investigated using UV-vis-NIR diffuse reflectance spectroscopy in an aim to study its potentiality as photocatalysts. Absorption spectra for the three double perovskites stabilized at 900°C are reported in Fig. 11. In the UV-visible range, the oxygen-to-metal charge transfer bands are observed at 400 nm corresponding to $\text{O}^{2-} \rightarrow \text{Co}^{3+}$, 280 nm corresponding to $\text{O}^{2-} \rightarrow \text{Ga}^{3+}$, of $\text{O}^{2-} \rightarrow \text{Nb}^{5+}$ at 200 nm as discussed in the earlier subsection. The increase of the absorption bands with respect to the cobalt content is a clear indication for cobalt incorporation into the perovskite structure. As the spin-forbidden d-d transitions have poor maxima in the absorption curve, d-d transitions in the $\text{Sr}_2\text{Co}_x\text{Ga}_{1-x}\text{NbO}_6$ double perovskites ($x = 0.02, 0.04, 0.12$) is not assigned herein. The transitions are expected to be found at the wavelength values close to the ones discussed in Fig. 10 and, the presence of LS and HS/IS Co^{3+} were confirmed from ESR and NMR experiments respectively as shown in Fig. S5. Additionally, the features in the NIR range of absorption spectra (marked as \star in Fig. 11) correspond to the Jahn-Teller distortion are still observed. The features are more prominent in $x = 0.02$ sample. The increase in absorption with the cobalt content resulting in poorly make out the Jahn-Teller features in sample with more cobalt content than 4% .

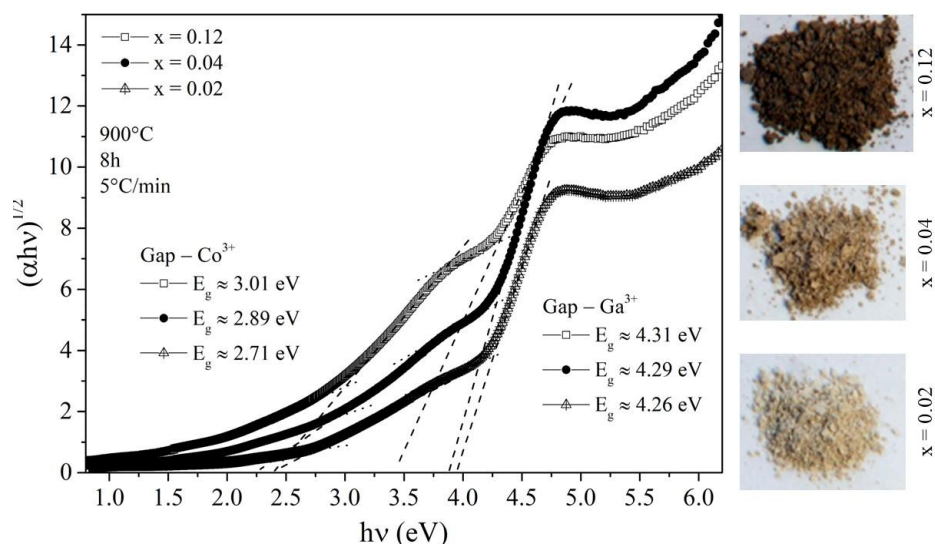


Fig. 12: Tauc plots for the $\text{Sr}_2(\text{Co}_x\text{Ga}_{1-x})\text{NbO}_6$ ($x = 0.02, 0.04$ and 0.12) double perovskites stabilized at a dwell temperature of 900°C with the sample photos.

Tauc plot for the calculation of band gap energy in $\text{Sr}_2(\text{Co}_x\text{Ga}_{1-x})\text{NbO}_6$ along with the sample photos is shown in Fig. 12. The Tauc method for analysing the UV-vis-NIR data is used in a number

of non-oxide^{70,71} and oxide⁷² ordered double perovskites (that show photocatalysis property as well^{39,60,73}). The Tauc plot for calculating direct band gap energy from the diffuse reflectance spectra is given by the following equation,

$$\alpha h\nu^{1/2} = B(h\nu - E_g)$$

where $\alpha = K/S = (1-R)^2/2R$, K and S are absorption and scattering coefficients respectively, R is the diffuse reflection recorded, h is Planck's constant, ν is the photon frequency, B is the proportionality constant and E_g is the band gap energy.⁷⁴ The intercept of the linear fit to the steep feature in the Tauc plot where $\alpha h\nu^{1/2} = 0$ gives the band gap energy. For materials which are doped, the band energy is taken at the energy value where the linear fit of the steep region in the absorption and the baseline meets. The dotted lines in Fig. 12 represent the baseline and the dashed lines corresponds to the linear fit of the steep feature.⁷⁵ $\text{Sr}_2(\text{Co}_x\text{Ga}_{1-x})\text{NbO}_6$ double perovskite was found to show two sub-band gap energies; one related to Ga^{3+} and the other related to the Co substitution. Insulators show band gap energy, $E_g > 4$ eV and is as reported for Gallium oxides.⁷⁶ Both the sub-band gap energies increase with the cobalt content. The band gap energy related to the cobalt in the double perovskite under study with $E_g < 4$ eV could make the double perovskite $\text{Sr}_2(\text{Co}_x\text{Ga}_{1-x})\text{NbO}_6$ an interesting candidate for photocatalytic studies.

Discussion

As mentioned earlier, the flux method was primarily and extensively used in the past for single crystal growth process. However, the molten flux method of synthesizing has been successful in preparing phase pure multicationic oxides such as LaCoO_3 using a eutectic mixture of NaCl-KCl ⁷⁷, Sr_2AlBO_6 (B=Nb, Ta) using SrCl_2 flux^{67,78}, SrTiO_3 using NaCl ⁴⁵, KF-LiF and K-Li-borate fluxes⁷⁹. The synthesis method provides a temperature range of preparation comparatively lower and a faster mass transport & nucleation process over the conventional solid-state method of synthesizing perovskites.^{58,77,80} The type of flux could be halide salt, oxosalt, hydroxide, carbonate, nitrate, sulfate to name a few.⁸¹ Compared to the other methods of synthesis for the perovskites which are either expensive or strenuous multiple grinding and heat treatments involved, use of flux for preparing the materials reduces the cost, time, and effort to synthesize the same materials using the other modes of preparation. In molten salt flux method, the mixture of salt and reagents is heated to a temperature between the melting and boiling point of the salt. When the salt is melted, it acts as a solvent system which allows the reagents to mix at a lower temperature and a faster diffusion rate than the usual synthesis methods. Thus, a flux must: (1) have no reactivity to the reagents and the crucible, (2) be easily removed once the desired product is formed at the end of a reaction, (3) be of low cost, volatility, and melting point.^{82,83} The nature of flux, reaction temperature and time, ratio of flux to product are system specific.^{77,78} Nonetheless, flux having a common cation or anion has a favorable impact on forming the phase-pure product.⁸³ A representative RT PXRD pattern for $\text{Sr}_2(\text{Co}_x\text{Ga}_{1-x})$

x)NbO₆ double perovskite prepared via conventional solid state route (marked as “without flux” in Fig. 13) and molten-flux method (marked as “with flux” in Fig. 13) under the same synthesis conditions (900°C dwell temperature for 16 hours of dwell time at 5°C/min cooling rate and cobalt content, $x = 0.08$) is shown in Fig. 13. ★ corresponds to the unwanted phases arising when the sample was prepared without flux. It can be easily deciphered from Fig. 13 that along with the desired phase there were other phases forming with the use of conventional solid-state synthesis route in contrast to the molten-flux method which stabilized the desired double perovskite phase at comparatively low reaction temperature as 900°C.

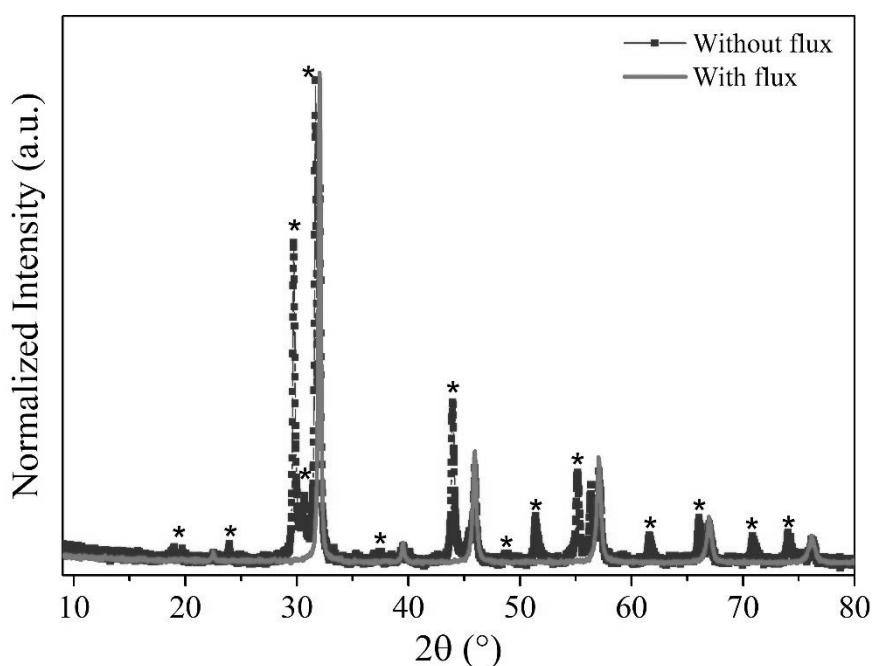


Fig. 13: Representative Sr₂(Co_xGa_{1-x})NbO₆ ($x = 0.08$) prepared at 900°C for 16 hours with a cooling rate of 5°C/min with and without flux (SrCl₂; 2:1 flux:sample). ★ corresponds to the unwanted phase(s).

In Sr₂Co_{0.04}Ga_{0.96}NbO₆ double perovskite (900°C, 72h, 0.2°C/min), our assumption of Co³⁺ occupied Ga³⁺ site as desired during the Rietveld refinement of PXRD pattern supported by NMR results is agreeable with HS/LS Co³⁺ occupation at Ga³⁺ site because of the same charge (+3) than to Nb⁵⁺ site. Also, the chemical bond nature (Nb electronegativity is lower than the Ga and Co one's so one expect a higher covalency for Ga(Co)-O bonds regarding the Nb-O one's) can be another for the Co occupation at Ga site. These assumptions were justified based on the NMR results of Sr₂Co_{0.04}Ga_{0.96}NbO₆ double perovskite (900°C, 72h, 0.2°C/min). Regarding the synthesis parameter study, it is clear that each set of parameters need to be refined for each x , cobalt content. However, two tendencies emerge concerning the rates of chemical reactions. First, when the dwell temperature is at

lowest, i.e., at 900°C, both the dwell time and the cooling rate should be longer (72 hours and 0.2°C/min respectively). Secondly, when the dwell temperature is at highest, i.e., at 1100°C, the dwell time could be reduced to at least 8h and a comparatively moderate cooling rate of 5°C/min. Sr₂Co_{0.04}Ga_{0.96}NbO₆ prepared with the following synthesis conditions: 900°C, 72h, 0.2°C/min was found to be crystallized in cubic space group (*Fm* $\bar{3}$ *m*). However, there is a competition between crystallization of Sr₂Co_xGa_{1-x}NbO₆ double perovskite in cubic (*Fm* $\bar{3}$ *m*) and tetragonal (*I4/m*) space group symmetry as in the Sr₂CoNbO₆⁶⁴ double perovskite matrix. Sr₂Co_{0.02}Ga_{0.98}NbO₆ in Fig. 11 have shown the features in the NIR range that correspond to the Jahn-Teller distortion which suggests that the double perovskite could have a tetragonal (*I4/m*) space group symmetry coming from microcrystallites. However, the cubic crystal symmetry (coming from the nanocrystallites) might be an effect of the small distortion that is averaged out in PXRD pattern and the matrix constraints the cooperative Jahn-Teller distortion in the sample.

Perovskite metal oxides have already proven to be efficient photocatalysts under UV and visible light.⁸⁴⁻⁸⁷ Moreover, transition metal doping has proven to enhance the photocatalytic properties as noted earlier.²¹ Additionally, studies have shown that the oxide double perovskites are a promising class of materials to be a photocatalyst for water splitting.^{60,88} Furthermore, perovskite metal oxide photocatalyst preparation via flux method had been of research focus.⁸² Therefore, herein, we reported a transition metal doped ordered double perovskite Sr₂Co_xGa_{1-x}NbO₆ that has the potential for photocatalysis under visible light synthesized via molten-salt flux method. The reported double perovskites in this article with a band gap energy less than 4 eV is prospective photocatalysts that can degrade and treat a plethora of chemical effluents and/or disinfect water.⁸⁹ The sub-band gap energy related to the cobalt substitution was found to be increasing with the cobalt content, x, which reaffirms the studies that concluded Co as the most promising dopant to enhance the photocatalytic properties than the pristine counterparts.

Conclusion

The double perovskite Sr₂Co_xGa_{1-x}NbO₆ was found to have stabilized with a cost and time efficient synthesis strategy of molten-salt flux method. The refinement of the heat treatment parameters to solve the quest of finding the right parameters for phase-pure Sr₂Co_xGa_{1-x}NbO₆ was carried out. It was found that phase-pure sample was able to synthesis for the cobalt substitution content, x = 0.04 with the good thermal parameters of 900°C dwell temperature, 72 hours dwell time and 0.2°C/min cooling rate using SrCl₂ flux in a 2:1 flux:product ratio under air. This pale brown material, which showed a mixed spin state at room temperature, is a potential candidate for inorganic “cool” pigment. The optical study performed on a set of cobalt content values, x = 0.02, 0.04 and 0.12 showed that these Sr₂Co_xGa_{1-x}NbO₆ double perovskites have the potentiality to be used as photocatalysts for water splitting.

Acknowledgement

The authors OT and MV would like to thank Université de Bordeaux for the PhD thesis funding, Dr. F. Weill (Placamat, Bordeaux) for electron diffraction measurement, Dr. M. Gaudon (ICMCB, Bordeaux) and Dr. D. Carlier (ICMCB, Bordeaux) for their valuable insights on spectroscopy analysis. MV and OT thank Bakary Camara for synthesizing some samples during his undergraduate internship that helped the study in this article. OT would thanks MAAF, SGM and EMM from Inorganic Chemistry department (Complutense University of Madrid) for all the fruitful exchanges.

References

- (1) Desore, A.; Narula, S. A. An Overview on Corporate Response towards Sustainability Issues in Textile Industry. *Environment, Development and Sustainability* **2018**, *20* (4), 1439–1459. <https://doi.org/10.1007/s10668-017-9949-1>.
- (2) Bhatia, S. C.; Devraj, S. *Pollution Control in Textile Industry*, 1st ed.; WPI Publishing: New York, 2017.
- (3) Setiadi, T.; Andriani, Y.; Erlania, M. Treatment of Textile Wastewater by a Combination of Anaerobic and Aerobic Processes: A Denim Processing Plant Case. *The First International Symposium on Southeast Asian Water Environment* **2003**, *8*. From Ohgaki, Shinichiro, and Kensuke Fukushi. “Southeast Asian Water Environment 1 : Selected Papers from the First International Symposium on Southeast Asian Water Environment (biodiversity and Water Environment), Bangkok, Thailand, October 2003 / Edited by Shinichiro Ohgaki with Kensuke Fukushi [and Three Others].” Ed. Shinichiro Ohgaki and Kensuke Fukushi. London: IWA Publishing, 2006. Print.
- (4) Hassan, M. M.; Carr, C. M. A Critical Review on Recent Advancements of the Removal of Reactive Dyes from Dyehouse Effluent by Ion-Exchange Adsorbents. *Chemosphere* **2018**, *209*, 201–219. <https://doi.org/10.1016/j.chemosphere.2018.06.043>.
- (5) Imran, M.; Crowley, D. E.; Khalid, A.; Hussain, S.; Mumtaz, M. W.; Arshad, M. Microbial Biotechnology for Decolorization of Textile Wastewaters. *Rev Environ Sci Biotechnol* **2015**, *14* (1), 73–92. <https://doi.org/10.1007/s11157-014-9344-4>.
- (6) Sandhya, S. Biodegradation of Azo Dyes Under Anaerobic Condition: Role of Azoreductase. In *Biodegradation of Azo Dyes*; Atacag Erkurt, H., Ed.; The Handbook of Environmental Chemistry; Springer: Berlin, Heidelberg, 2010; pp 39–57. https://doi.org/10.1007/698_2009_43.
- (7) Newman, M. C. *Fundamentals of Ecotoxicology : The Science of Pollution, Fourth Edition*, 4th ed.; CRC Press: Boca Raton, 2014. <https://doi.org/10.1201/b17658>.
- (8) Orts, F.; del Río, A. I.; Molina, J.; Bonastre, J.; Cases, F. Electrochemical Treatment of Real Textile Wastewater: Trichromy Procion HEXL®. *Journal of Electroanalytical Chemistry* **2018**, *808*, 387–394. <https://doi.org/10.1016/j.jelechem.2017.06.051>.
- (9) Jordão, C.; Puppim, R.; Broega, A. C. Solutions Notes on Clean Textile Waste. In *Innovation, Engineering and Entrepreneurship*; Machado, J., Soares, F., Veiga, G., Eds.; Lecture Notes in Electrical Engineering; Springer International Publishing: Cham, 2019; pp 682–689. https://doi.org/10.1007/978-3-319-91334-6_93.
- (10) Delée, W.; O'Neill, C.; Hawkes, F. R.; Pinheiro, H. M. Anaerobic Treatment of Textile Effluents: A Review. *Journal of Chemical Technology & Biotechnology* **1998**, *73* (4), 323–335. [https://doi.org/10.1002/\(SICI\)1097-4660\(199812\)73:4<323::AID-JCTB976>3.0.CO;2-S](https://doi.org/10.1002/(SICI)1097-4660(199812)73:4<323::AID-JCTB976>3.0.CO;2-S).
- (11) Wu, G.; Yin, Q. Microbial Niche Nexus Sustaining Biological Wastewater Treatment. *npj Clean Water* **2020**, *3*, 1–6. <https://doi.org/10.1038/s41545-020-00080-4>.
- (12) Hodges, B. C.; Cates, E. L.; Kim, J.-H. Challenges and Prospects of Advanced Oxidation Water Treatment Processes Using Catalytic Nanomaterials. *Nature Nanotechnology* **2018**, *13* (8), 642–650. <https://doi.org/10.1038/s41565-018-0216-x>.
- (13) Liu, P.; Li, C.; Zhao, Z.; Lu, G.; Cui, H.; Zhang, W. Induced Effects of Advanced Oxidation Processes. *Scientific Reports* **2014**, *4* (1), 4018. <https://doi.org/10.1038/srep04018>.
- (14) Jain, A.; He, Z. Cathode-Enhanced Wastewater Treatment in Bioelectrochemical Systems. *npj Clean Water* **2018**, *1* (1), 1–5. <https://doi.org/10.1038/s41545-018-0022-x>.
- (15) Cakir, F. Y.; Stenstrom, M. K. Greenhouse Gas Production: A Comparison between Aerobic and Anaerobic Wastewater Treatment Technology. *Water Research* **2005**, *39* (17), 4197–4203. <https://doi.org/10.1016/j.watres.2005.07.042>.
- (16) Santhosh, C.; Malathi, A.; Daneshvar, E.; Kollu, P.; Bhatnagar, A. Photocatalytic Degradation of Toxic Aquatic Pollutants by Novel Magnetic 3D-TiO₂@HPGA Nanocomposite. *Scientific Reports* **2018**, *8*, 15531. <https://doi.org/10.1038/s41598-018-33818-9>.
- (17) Gupta, N. K.; Ghaffari, Y.; Kim, S.; Bae, J.; Kim, K. S.; Saifuddin, M. Photocatalytic Degradation of Organic Pollutants over MFe₂O₄ (M = Co, Ni, Cu, Zn) Nanoparticles at Neutral PH. *Scientific Reports* **2020**, *10*, 4942. <https://doi.org/10.1038/s41598-020-61930-2>.

- (18) Muhd Julkapli, N.; Bagheri, S.; Bee Abd Hamid, S. Recent Advances in Heterogeneous Photocatalytic Decolorization of Synthetic Dyes. *The Scientific World Journal* **2014**, *2014*, 25. <https://doi.org/10.1155/2014/692307>.
- (19) Adeel, M.; Saeed, M.; Khan, I.; Muneer, M.; Akram, N. Synthesis and Characterization of Co–ZnO and Evaluation of Its Photocatalytic Activity for Photodegradation of Methyl Orange. *ACS Omega* **2021**, *6* (2), 1426–1435. <https://doi.org/10.1021/acsomega.0c05092>.
- (20) Shindhal, T.; Rakholiya, P.; Varjani, S.; Pandey, A.; Ngo, H. H.; Guo, W.; Ng, H. Y.; Taherzadeh, M. J. A Critical Review on Advances in the Practices and Perspectives for the Treatment of Dye Industry Wastewater. *Bioengineered* **2020**, *12* (1), 70–87. <https://doi.org/10.1080/21655979.2020.1863034>.
- (21) Joseph, D. P.; Venkateswaran, C. Bandgap Engineering in ZnO By Doping with 3d Transition Metal Ions. *Journal of Atomic and Molecular Physics* **2011**, *2011* (270540), 7.
- (22) Wilke, K.; Breuer, H. D. The Influence of Transition Metal Doping on the Physical and Photocatalytic Properties of Titania. *Journal of Photochemistry and Photobiology A: Chemistry* **1999**, *121* (1), 49–53. [https://doi.org/10.1016/S1010-6030\(98\)00452-3](https://doi.org/10.1016/S1010-6030(98)00452-3).
- (23) Goswami, N.; Sahai, A. Structural Transformation in Nickel Doped Zinc Oxide Nanostructures. *Materials Research Bulletin* **2013**, *48* (2), 346–351. <https://doi.org/10.1016/j.materresbull.2012.10.045>.
- (24) Altintas Yildirim, O.; Arslan, H.; Sönmezoğlu, S. Facile Synthesis of Cobalt-Doped Zinc Oxide Thin Films for Highly Efficient Visible Light Photocatalysts. *Applied Surface Science* **2016**, *390*, 111–121. <https://doi.org/10.1016/j.apsusc.2016.08.069>.
- (25) Polat, İ.; Yılmaz, S.; Altın, İ.; Bacaksız, E.; Sökmen, M. The Influence of Cu-Doping on Structural, Optical and Photocatalytic Properties of ZnO Nanorods. *Materials Chemistry and Physics* **2014**, *148* (3), 528–532. <https://doi.org/10.1016/j.matchemphys.2014.07.011>.
- (26) Jug, K.; Tikhomirov, V. A. Comparative Studies of Cation Doping of ZnO with Mn, Fe, and Co. *The Journal of Physical Chemistry A* **2009**, *113* (43), 11651–11655. <https://doi.org/10.1021/jp902532a>.
- (27) Lu, Y.; Lin, Y.; Wang, D.; Wang, L.; Xie, T.; Jiang, T. A High Performance Cobalt-Doped ZnO Visible Light Photocatalyst and Its Photogenerated Charge Transfer Properties. *Nano Res.* **2011**, *4* (11), 1144–1152. <https://doi.org/10.1007/s12274-011-0163-4>.
- (28) He, R.; Hocking, R. K.; Tsuzuki, T. Local Structure and Photocatalytic Property of Sol–Gel Synthesized ZnO Doped with Transition Metal Oxides. *J Mater Sci* **2011**, *47* (7), 3150–3158. <https://doi.org/10.1007/s10853-011-6149-5>.
- (29) Xiao, Q.; Zhang, J.; Xiao, C.; Tan, X. Photocatalytic Decolorization of Methylene Blue over Zn_{1-x}CoxO under Visible Light Irradiation. *Materials Science and Engineering: B* **2007**, *142* (2–3), 121–125. <https://doi.org/10.1016/j.mseb.2007.06.021>.
- (30) Kuriakose, S.; Satpati, B.; Mohapatra, S. Enhanced Photocatalytic Activity of Co Doped ZnO Nanodisks and Nanorods Prepared by a Facile Wet Chemical Method. *Phys. Chem. Chem. Phys.* **2014**, *16* (25), 12741–12749. <https://doi.org/10.1039/C4CP01315H>.
- (31) Patel, P. P.; Hanumantha, P. J.; Velikokhatnyi, O. I.; Datta, M. K.; Hong, D.; Gattu, B.; Poston, J. A.; Manivannan, A.; Kumta, P. N. Nitrogen and Cobalt Co-Doped Zinc Oxide Nanowires – Viable Photoanodes for Hydrogen Generation via Photoelectrochemical Water Splitting. *Journal of Power Sources* **2015**, *299*, 11–24. <https://doi.org/10.1016/j.jpowsour.2015.08.027>.
- (32) Gonçalves, N. P. F.; Paganini, M. C.; Armillotta, P.; Cerrato, E.; Calza, P. The Effect of Cobalt Doping on the Efficiency of Semiconductor Oxides in the Photocatalytic Water Remediation. *Journal of Environmental Chemical Engineering* **2019**, *7* (6), 103475. <https://doi.org/10.1016/j.jece.2019.103475>.
- (33) Šutka, A.; Käämbre, T.; Pärna, R.; Juhneviča, I.; Maiorov, M.; Joost, U.; Kisand, V. Co Doped ZnO Nanowires as Visible Light Photocatalysts. *Solid State Sciences* **2016**, *56*, 54–62. <https://doi.org/10.1016/j.solidstatesciences.2016.04.008>.
- (34) Kumar, Y.; Sahai, A.; Olive-Méndez, S. F.; Goswami, N.; Agarwal, V. Morphological Transformations in Cobalt Doped Zinc Oxide Nanostructures: Effect of Doping Concentration. *Ceramics International* **2016**, *42* (4), 5184–5194. <https://doi.org/10.1016/j.ceramint.2015.12.041>.

- (35) Lee, H.; Park, Y.-K.; Kim, S.-J.; Kim, B.-H.; Jung, S.-C. Titanium Dioxide Modification with Cobalt Oxide Nanoparticles for Photocatalysis. *Journal of Industrial and Engineering Chemistry* **2015**, *32*, 259–263. <https://doi.org/10.1016/j.jiec.2015.08.025>.
- (36) Rajbongshi, B. M.; Samdarshi, S. K. ZnO and Co-ZnO Nanorods—Complementary Role of Oxygen Vacancy in Photocatalytic Activity of under UV and Visible Radiation Flux. *Materials Science and Engineering: B* **2014**, *182*, 21–28. <https://doi.org/10.1016/j.mseb.2013.11.013>.
- (37) Yin, W.-J.; Weng, B.; Ge, J.; Sun, Q.; Li, Z.; Yan, Y. Oxide Perovskites, Double Perovskites and Derivatives for Electrocatalysis, Photocatalysis, and Photovoltaics. *Energy Environ. Sci.* **2019**, *12* (2), 442–462. <https://doi.org/10.1039/C8EE01574K>.
- (38) Weng, B.; Grice, C. R.; Ge, J.; Poudel, T.; Deng, X.; Yan, Y. Barium Bismuth Niobate Double Perovskite/Tungsten Oxide Nanosheet Photoanode for High-Performance Photoelectrochemical Water Splitting. *Advanced Energy Materials* **2018**, *8* (10), 1701655. <https://doi.org/10.1002/aenm.201701655>.
- (39) Idris, A. M.; Liu, T.; Hussain Shah, J.; Malik, A. S.; Zhao, D.; Han, H.; Li, C. Sr₂NiWO₆ Double Perovskite Oxide as a Novel Visible-Light-Responsive Water Oxidation Photocatalyst. *ACS Applied Materials & Interfaces* **2020**, *12* (23), 25938–25948. <https://doi.org/10.1021/acsami.0c05576>.
- (40) Hwang, J.; Rao, R. R.; Giordano, L.; Katayama, Y.; Yu, Y.; Shao-Horn, Y. Perovskites in Catalysis and Electrocatalysis. *Science* **2017**, *358* (6364), 751–756. <https://doi.org/10.1126/science.aam7092>.
- (41) Arney, D.; Hardy, C.; Greve, B.; Maggard, P. A. Flux Synthesis of AgNbO₃: Effect of Particle Surfaces and Sizes on Photocatalytic Activity. *Journal of Photochemistry and Photobiology A: Chemistry* **2010**, *214* (1), 54–60. <https://doi.org/10.1016/j.jphotochem.2010.06.006>.
- (42) Arney, D.; Watkins, T.; Maggard, P. A. Effects of Particle Surface Areas and Microstructures on Photocatalytic H₂ and O₂ Production over PbTiO₃. *Journal of the American Ceramic Society* **2011**, *94* (5), 1483–1489. <https://doi.org/10.1111/j.1551-2916.2010.04262.x>.
- (43) Noureldine, D.; Anjum, D. H.; Takanabe, K. Flux-Assisted Synthesis of SnNb₂O₆ for Tuning Photocatalytic Properties. *Phys. Chem. Chem. Phys.* **2014**, *16* (22), 10762–10769. <https://doi.org/10.1039/C4CP00654B>.
- (44) Porob, D. G.; Maggard, P. A. Flux Syntheses of La-Doped NaTaO₃ and Its Photocatalytic Activity. *Journal of Solid State Chemistry* **2006**, *179* (6), 1727–1732. <https://doi.org/10.1016/j.jssc.2006.03.008>.
- (45) Kato, H.; Kobayashi, M.; Hara, M.; Kakihana, M. Fabrication of SrTiO₃ Exposing Characteristic Facets Using Molten Salt Flux and Improvement of Photocatalytic Activity for Water Splitting. *Catal. Sci. Technol.* **2013**, *3* (7), 1733–1738. <https://doi.org/10.1039/C3CY00014A>.
- (46) Toulemonde, O.; Devoti, A.; Rosa, P.; Guionneau, P.; Duttine, M.; Wattiaux, A.; Lebraud, E.; Penin, N.; Decourt, R.; Fargues, A.; Buffière, S.; Demourgues, A.; Gaudon, M. Probing Co- and Fe-Doped LaMO₃ (M = Ga, Al) Perovskites as Thermal Sensors. *Dalton Transactions* **2018**, *47* (2), 382–393. <https://doi.org/10.1039/C7DT03647G>.
- (47) Haverkort, M. W.; Hu, Z.; Cezar, J. C.; Burnus, T.; Hartmann, H.; Reuther, M.; Zobel, C.; Lorenz, T.; Tanaka, A.; Brookes, N. B.; Hsieh, H. H.; Lin, H.-J.; Chen, C. T.; Tjeng, L. H. Spin State Transition in LaCoO₃ Studied Using Soft X-Ray Absorption Spectroscopy and Magnetic Circular Dichroism. *Phys. Rev. Lett.* **2006**, *97* (17), 176405. <https://doi.org/10.1103/PhysRevLett.97.176405>.
- (48) Korotin, M. A.; Ezhov, S. Yu.; Solovyev, I. V.; Anisimov, V. I.; Khomskii, D. I.; Sawatzky, G. A. Intermediate-Spin State and Properties of LaCoO₃. *Phys. Rev. B* **1996**, *54* (8), 5309–5316. <https://doi.org/10.1103/PhysRevB.54.5309>.
- (49) James, N. E. Temperature indicating container and lid apparatus. Patent number US5720555A, 1996. <https://patentcenter.uspto.gov/applications/08653135>
- (50) Pimia, J. Temperature Indicator for Temperature Changing Material or Means and Method for Its Preparation. Patent number US20130010827A1, January 10, 2013. <https://patentcenter.uspto.gov/applications/13637097>
- (51) Wang, X.; Mu, B.; Xu, J.; Wang, A. Reversible Thermochromic Superhydrophobic BiVO₄ Hybrid Pigments Coatings with Self-Cleaning Performance and Environmental Stability Based

- on Kaolinite. *ACS Appl. Mater. Interfaces* **2021**, *13* (2), 3228–3236. <https://doi.org/10.1021/acsami.0c20029>.
- (52) Cao, L.; Fang, L.; Li, X.; Chen, S.; Lu, C.; Xu, Z. Chameleon Inspired Layer-by-Layer Assembly of Thermochromic Microcapsules to Achieve Controllable Multiple-Color Change. *Smart Mater. Struct.* **2020**, *29* (4), 04LT02. <https://doi.org/10.1088/1361-665X/ab7945>.
- (53) Wanklyn, B. M. Flux Growth of Some Complex Oxide Materials. *Journal of Materials Science* **1972**, *7* (7), 813–821. <https://doi.org/10.1007/BF00549910>.
- (54) Wang, X.; Huang, K.; Yuan, L.; Li, S.; Ma, W.; Liu, Z.; Feng, S. Molten Salt Flux Synthesis, Crystal Facet Design, Characterization, Electronic Structure, and Catalytic Properties of Perovskite Cobaltite. *ACS Appl. Mater. Interfaces* **2018**, *10* (33), 28219–28231. <https://doi.org/10.1021/acsami.8b08621>.
- (55) Gonell, F.; Alem, N.; Dunne, P.; Crochet, G.; Beaunier, P.; Méthivier, C.; Montero, D.; Laberty-Robert, C.; Doudin, B.; Portehault, D. Versatile Molten Salt Synthesis of Manganite Perovskite Oxide Nanocrystals and Their Magnetic Properties. *ChemNanoMat* **2019**, *5* (3), 358–363. <https://doi.org/10.1002/cnma.201800632>.
- (56) Remeika, J. P.; Jackson, W. M. A Method for Growing Barium Titanate Single Crystals. *J. Am. Chem. Soc.* **1954**, *76* (3), 940–941. <https://doi.org/10.1021/ja01632a107>.
- (57) Nielsen, J. W.; Dearborn, E. F. The Growth of Single Crystals of Magnetic Garnets. *Journal of Physics and Chemistry of Solids* **1958**, *5* (3), 202–207. [https://doi.org/10.1016/0022-3697\(58\)90068-4](https://doi.org/10.1016/0022-3697(58)90068-4).
- (58) Elwell, D.; Neate, B. W. Mechanisms of Crystal Growth from Fluxed Melts. *Journal of Materials Science* **1971**, *6*, 1499–1519.
- (59) Vradman, L.; Zana, J.; Kirschner, A.; Herskowitz, M. Synthesis of LaMnO₃ in Molten Chlorides: Effect of Preparation Conditions. *Phys. Chem. Chem. Phys.* **2013**, *15* (26), 10914. <https://doi.org/10.1039/c3cp50713k>.
- (60) Idris, A. M.; Liu, T.; Shah, J. H.; Zhang, X.; Ma, C.; Malik, A. S.; Jin, A.; Rasheed, S.; Sun, Y.; Li, C.; Han, H. A Novel Double Perovskite Oxide Semiconductor Sr₂CoWO₆ as Bifunctional Photocatalyst for Photocatalytic Oxygen and Hydrogen Evolution Reactions from Water under Visible Light Irradiation. *Solar RRL* **2020**, *4* (3), 1900456. <https://doi.org/10.1002/solr.201900456>.
- (61) Varghese, M.; Simpson, S.; Lawrence, G.; Duttine, M.; Sanz Camacho, P.; Gaudon, M.; Toulemonde, O. Room-Temperature Mixed Spin State of Co³⁺ in Sr₂Co_{0.02}Ga_{0.98}NbO₆ Double Perovskites: Combined NMR and EPR Studies in a Potential Inorganic Pigment. *J. Phys. Chem. C* **2022**, *126* (19), 8450–8460. <https://doi.org/10.1021/acs.jpcc.2c00191>.
- (62) Ivanova, S.; Zhecheva, E.; Stoyanova, R. Microstructure of LaCoO₃ Prepared by Freeze-Drying of Metal–Citrate Precursors Revealed by EPR. *Journal of Physics and Chemistry of Solids* **2007**, *68* (2), 168–174. <https://doi.org/10.1016/j.jpcs.2006.10.005>.
- (63) Mesaros, A.; Ghitulica, C. D.; Popa, M.; Mereu, R.; Popa, A.; Petrisor, T.; Gabor, M.; Cadis, A. I.; Vasile, B. S. Synthesis, Structural and Morphological Characteristics, Magnetic and Optical Properties of Co Doped ZnO Nanoparticles. *Ceramics International* **2014**, *40* (2), 2835–2846. <https://doi.org/10.1016/j.ceramint.2013.10.030>.
- (64) Bashir, J.; Shaheen, R. Structural and Complex AC Impedance Spectroscopic Studies of A₂CoNbO₆ (A = Sr, Ba) Ordered Double Perovskites. *Solid State Sciences* **2011**, *13* (5), 993–999. <https://doi.org/10.1016/j.solidstatesciences.2011.02.003>.
- (65) Mitchell, R. H. *Perovskites: Modern and Ancient*; Almaz Press, 2002. (<http://www.minsocam.org/msa/almazpress/>)
- (66) Vasala, S.; Karppinen, M. A₂B'B''O₆ Perovskites: A Review. *Progress in Solid State Chemistry* **2015**, *43* (1–2), 1–36. <https://doi.org/10.1016/j.progsolidstchem.2014.08.001>.
- (67) Woodward, P.; Hoffmann, R.-D.; Sleight, A. W. Order-Disorder in A₂M³⁺M⁵⁺O₆ Perovskites. *Journal of Materials Research* **1994**, *9* (8), 2118–2127. <https://doi.org/10.1557/JMR.1994.2118>.
- (68) Iwakura, H.; Einaga, H.; Teraoka, Y. Relationship between Cation Arrangement and Photocatalytic Activity for Sr–Al–Nb–O Double Perovskite. *Inorganic Chemistry* **2010**, *49* (24), 11362–11369. <https://doi.org/10.1021/ic101208q>.

- (69) Sanz-Ortiz, M. N.; Rodríguez, F.; Rodríguez, J.; Demazeau, G. Optical and Magnetic Characterisation of Co^{3+} and Ni^{3+} in LaAlO_3 : Interplay between the Spin State and Jahn–Teller Effect. *Journal of Physics: Condensed Matter* **2011**, *23* (41), 415501. <https://doi.org/10.1088/0953-8984/23/41/415501>.
- (70) Liao, Q.; Chen, J.; Zhou, L.; Wei, T.; Zhang, L.; Chen, D.; Huang, F.; Pang, Q.; Zhang, J. Z. Bandgap Engineering of Lead-Free Double Perovskite $\text{Cs}_2\text{AgInCl}_6$ Nanocrystals via Cu^{2+} -Doping. *J. Phys. Chem. Lett.* **2020**, *11* (19), 8392–8398. <https://doi.org/10.1021/acs.jpcclett.0c02553>.
- (71) Wei, F.; Deng, Z.; Sun, S.; Xie, F.; Kieslich, G.; Evans, D. M.; Carpenter, M. A.; Bristowe, P. D.; Cheetham, A. K. The Synthesis, Structure and Electronic Properties of a Lead-Free Hybrid Inorganic–Organic Double Perovskite $(\text{MA})_2\text{KBiCl}_6$ (MA = Methylammonium). *Mater. Horiz.* **2016**, *3* (4), 328–332. <https://doi.org/10.1039/C6MH00053C>.
- (72) Shirazi, P.; Rahbar, M.; Behpour, M.; Ashrafi, M. $\text{La}_2\text{MnTiO}_6$ Double Perovskite Nanostructures as Highly Efficient Visible Light Photocatalysts. *New J. Chem.* **2019**, *44* (1), 231–238. <https://doi.org/10.1039/C9NJ04932K>.
- (73) Idris, A. M.; Liu, T.; Hussain Shah, J.; Han, H.; Li, C. $\text{Sr}_2\text{CoTaO}_6$ Double Perovskite Oxide as a Novel Visible-Light-Absorbing Bifunctional Photocatalyst for Photocatalytic Oxygen and Hydrogen Evolution Reactions. *ACS Sustainable Chem. Eng.* **2020**, *8* (37), 14190–14197. <https://doi.org/10.1021/acssuschemeng.0c05237>.
- (74) Pankove, J. I. *Optical Processes in Semiconductors*; Prentice-Hall; 1st Edition (January 1, 1971) ISBN-13 : 978-0136380238
- (75) Makuła, P.; Pacia, M.; Macyk, W. How To Correctly Determine the Band Gap Energy of Modified Semiconductor Photocatalysts Based on UV–Vis Spectra. *J. Phys. Chem. Lett.* **2018**, *9* (23), 6814–6817. <https://doi.org/10.1021/acs.jpcclett.8b02892>.
- (76) Pearton, S. J.; Ren, F.; Tadjer, M.; Kim, J. Perspective: Ga_2O_3 for Ultra-High Power Rectifiers and MOSFETS. *Journal of Applied Physics* **2018**, *124* (22), 220901. <https://doi.org/10.1063/1.5062841>.
- (77) Sanzhao, S.; Jian, S.; Jing, Z.; Chengzhi, G.; Zhiwei, H.; Ting-Shan, C.; Xian-Long, D.; Xiao, L.; Jun, H.; Linjuan, Z.; Jian-Qiang, W. Growth of LaCoO_3 Crystals in Molten Salt: Effects of Synthesis Conditions. *CrystEngComm* **2018**, *20* (15), 2093–2101. <https://doi.org/10.1039/D0CE01330G>
- (78) Goodenough, J. B.; Gräper, W.; Holtzberg, F.; Huber, D. L.; Lefever, R. A.; Longo, J. M.; McGuire, T. R.; Methfessel, S. *Magnetic and Other Properties of Oxides and Related Compounds*; Condensed Matter; Springer-Verlag: Berlin Heidelberg, 1970.
- (79) Scheel, H. J.; Bednorz, J. G.; Dill, P. Crystal Growth of Strontium Titanate SrTiO_3 . *Ferroelectrics* **1976**, *13* (1), 507–509. <https://doi.org/10.1080/00150197608236653>.
- (80) Elwell, D.; Scheel, H. J. *Crystal Growth from High-Temperature Solutions*; Report; ETH Zurich, 2011. <https://doi.org/10.3929/ethz-a-006779537> (<https://www.research-collection.ethz.ch/handle/20.500.11850/153060>)
- (81) Liu, X.; Fechler, N.; Antonietti, M. Salt Melt Synthesis of Ceramics, Semiconductors and Carbon Nanostructures. *Chem. Soc. Rev.* **2013**, *42* (21), 8237–8265. <https://doi.org/10.1039/C3CS60159E>.
- (82) Boltersdorf, J.; King, N.; Maggard, P. A. Flux-Mediated Crystal Growth of Metal Oxides: Synthetic Tunability of Particle Morphologies, Sizes, and Surface Features for Photocatalysis Research. *CrystEngComm* **2015**, *17* (11), 2225–2241. <https://doi.org/10.1039/C4CE01587H>.
- (83) Bugaris, D. E.; zur Loye, H.-C. Materials Discovery by Flux Crystal Growth: Quaternary and Higher Order Oxides. *Angewandte Chemie International Edition* **2012**, *51* (16), 3780–3811. <https://doi.org/10.1002/anie.201102676>.
- (84) Idris, A. M.; Liu, T.; Shah, J. H.; Malik, A. S.; Zhao, D.; Han, H.; Li, C. Sr_2NiWO_6 Double Perovskite Oxide as a Novel Visible-Light-Responsive Water Oxidation Photocatalyst. *ACS Applied Materials & Interfaces* **2020**. <https://doi.org/10.1021/acsami.0c05576>.
- (85) Grimaud, A.; May, K. J.; Carlton, C. E.; Lee, Y.-L.; Risch, M.; Hong, W. T.; Zhou, J.; Shao-Horn, Y. Double Perovskites as a Family of Highly Active Catalysts for Oxygen Evolution in Alkaline Solution. *Nat Commun* **2013**, *4* (1), 2439. <https://doi.org/10.1038/ncomms3439>.

- (86) Zhang, G.; Liu, G.; Wang, L.; Irvine, J. T. S. Inorganic Perovskite Photocatalysts for Solar Energy Utilization. *Chem. Soc. Rev.* **2016**, *45* (21), 5951–5984. <https://doi.org/10.1039/C5CS00769K>.
- (87) Li, S.; Zhang, Y.; Yang, W.; Liu, H.; Fang, X. 2D Perovskite Sr₂Nb₃O₁₀ for High-Performance UV Photodetectors. *Advanced Materials* **2020**, *32* (7), 1905443. <https://doi.org/10.1002/adma.201905443>.
- (88) Castelli, I. E.; Olsen, T.; Datta, S.; Landis, D. D.; Dahl, S.; Thygesen, K. S.; Jacobsen, K. W. Computational Screening of Perovskite Metal Oxides for Optimal Solar Light Capture. *Energy Environ. Sci.* **2012**, *5* (2), 5814–5819. <https://doi.org/10.1039/C1EE02717D>.
- (89) Ojha, A. Chapter 19 - Nanomaterials for Removal of Waterborne Pathogens: Opportunities and Challenges. In *Waterborne Pathogens*; Vara Prasad, M. N., Grobelak, A., Eds.; Butterworth-Heinemann, 2020; pp 385–432. <https://doi.org/10.1016/B978-0-12-818783-8.00019-0>.